

Redox capacity of rocks and sediments by high temperature chalcometric titration

Matthieu E. Galvez^{a,b,1,*}, Samuel L. Jaccard^{c,1}

^a Institute of Geochemistry and Petrology, Department of Earth Sciences, ETH Zurich, Zurich, Switzerland

^b The Branco Weiss/Society in Science Fellowship, ETH Zurich, Zurich, Switzerland

^c Institute of Geological Sciences and Oeschger Center for Climate Change Research, University of Bern, Bern, Switzerland

ARTICLE INFO

Editor: Christian France-lanord

ABSTRACT

We present an analytical method to quantify the absolute redox capacity, ΔO_2 , of geological materials. The protocol consists in a high temperature chalcometric titration by which a known amount of oxygen gas is exchanged between a solid state oxygen donor, CuO, and an oxygen acceptor, the sample, at elevated temperature. Calibration of the method using elemental C, native S and magnetite demonstrates that it effectively oxidizes C, S and Fe to their terminal oxidation state, C^{4+} , S^{6+} and Fe^{3+} , respectively. Because the metric is independent of processes of internal equilibration within the system, it can be used for quantitative assessments of redox fluxes in open geological systems, in the surface or deep Earth. Preliminary results suggest that the mass specific redox capacity, dO_2 , of geological materials span many orders of magnitude, ranging from less than 500 $\mu\text{mol O}_2/\text{g}$ for ultramafic rocks and lower crustal amphibolites, to more than 30000 $\mu\text{mol O}_2/\text{g}$ for black shales. This highlights a counterintuitive yet fundamental characteristic of our planet. Rocks characterized by elevated dO_2 values are ubiquitous in the oxic Earth's surface, while the upper mantle and lower crust are typically composed of rocks with much lower dO_2 . This work will contribute to provide a more nuanced and complete perspective on the sedimentary and geodynamic processes that have shaped the redox structure of the Earth.

1. Introduction

Reduction and oxidation (redox) reactions are at the core of many physiological processes (Borch et al., 2010; Kappler et al., 2004; Rimmer et al., 2006; Moore et al., 2017), and they also shape the long-term history of the Earth system (Falkowski et al., 2008; Falkowski and Godfrey, 2008; Frost and McCammon, 2008; Kleidon, 2010; Moore et al., 2017; Wood et al., 1990; Galvez et al., 2020). Over geological timescales, the flux of redox-sensitive elements including H, C, N, S, Fe, and Mn, between surface and deep reservoirs (Frost and McCammon, 2008; McCammon, 2005; Galvez, 2020) have mediated a planetary-scale differentiation in redox state (chemical potential of oxygen, μO_2) which is a hallmark of our planet. The μO_2 in the Earth's interior is significantly lower today than that of the O_2 -saturated ocean and atmosphere (Arculus, 1985; Frost and McCammon, 2008; McCammon, 2005).

The chemical potential of O_2 , and related variables such as the activity and fugacity of O_2 , is commonly used to describe the redox state of geological structures (Arculus, 1985; Frost and McCammon, 2008;

McCammon, 2005). It is an essential thermodynamic variable driving the transfer of oxidants and reductants between two systems at a given pressure (P) and temperature (T). But, it provides only a partial view of the redox characteristics and sensitivity of a geological system. First, because it is a thermodynamic potential, μO_2 depends on processes of internal equilibration between the different phases (e.g. fluid rock interaction), and can only be defined at a given P and T (e.g. Connolly, 1995). As a result, it has no absolute value as a comparative redox variable across all possible Earth environments. Second, chemical potentials depend primarily on the nature of the phase assemblage within a system (minerals, fluids etc.), and only marginally on the abundance and valence state of its elements. Hence, redox potentials do not reflect mass balance constraints associated with the chemical or mechanical exchange of oxidants/reductants between two systems, whether those exchanges occur at, or far from thermodynamic equilibrium. They are inadequate, in particular, to address questions such as (i) how much O_2 equivalents would a given lithology (e.g. peridotite, marine sediment etc.) consume from the atmosphere-ocean if it is allowed to fully react

* Corresponding author at: Department of Earth Sciences, ETH Zurich, Zurich, Switzerland.

E-mail addresses: matthieu.galvez@erdw.ethz.ch, matthieu.galvez@gmail.com (M.E. Galvez).

¹ Now at Institute of Earth Sciences, University of Lausanne, Lausanne, Switzerland.

<https://doi.org/10.1016/j.chemgeo.2020.120016>

Received 12 April 2020; Received in revised form 16 November 2020; Accepted 1 December 2020

Available online 3 December 2020

0009-2541/© 2020 The Authors.

Published by Elsevier B.V. This is an open access article under the CC BY-NC-ND license

(<http://creativecommons.org/licenses/by-nc-nd/4.0/>).

with it (i.e. oxidative weathering)? (ii) what is the net output of O_2 associated with reduced S burial in marine sediments? (iii) are subduction zones redox neutral (Evans, 2012; Galvez, 2020; Hayes and Waldbauer, 2006)?

To shed light on these sort of problems, a compositional redox variable is more appropriate because its definition does not require thermodynamic equilibrium to be established within the system, and it is also independent of environmental condition. The absolute redox capacity, or absolute electron-donor capacity (ΔO_2), which we operationally define here as the amount of O_2 required to oxidize the redox-active elements of a system to their highest attainable valence state under some reference condition, meets this requirement. Several authors (Connolly, 1995; Evans, 2006; Evans, 2012; Tumiati et al., 2015, and reference therein) have advocated for the use of compositional variables in dealing with redox-related questions. Yet, there exists no direct laboratory quantification of a rock's redox capacity, and therefore applications have relied on tedious compilation of disparate geochemical measurements.

Quantifying redox fluxes, e.g. net changes in redox capacity, has been notoriously difficult (Evans, 2006) because redox reactions often affect multiple elements simultaneously and are interwoven. The absolute redox capacity of a petrological system is usually estimated by combining data of redox-sensitive elements abundances, and valence state (Evans, 2006), but those data are obtained separately. Elemental compositions (including total organic carbon values) are determined by standard geochemical methods, while the valence state is assessed via element-specific spectroscopic approaches such as electron microprobe or Mossbauer spectroscopy (Evans et al., 2012), aqueous chemistry (Bézos and Humler, 2005), and/or synchrotron XANES for Fe^{2+}/Fe^{3+} (Berry et al., 2018; O'Neill et al., 2018; Waychunas et al., 1983; Wilke et al., 2001), and by acid-separation methods (Canfield et al., 1986; Morse and Cornwell, 1987) or synchrotron XANES for S species (Debret et al., 2017; Jugo et al., 2010; Waldo et al., 1991). Several examples of inventories, sometimes called *O_2 use*, *redox budget*, or *oxygen excess/deficit*, can be found in the literature (Alt et al., 2007; Brounce et al., 2019; Catling, 2014; Evans, 2012; Hayes and Waldbauer, 2006; Holland, 2002; Galvez, 2020; Tumiati et al., 2015). However, they remain relatively rare due to the complexity of compiling them.

Another method based on oxidative pyrolysis aimed to determine the total combustion oxygen demand (COD) of deep-sea sediments (Perks and Keeling, 1998; Perks et al., 2002). However, applications of the method have relied on the assumption that the oxidation of labile organic carbon dominates the signal, which may not be valid for depositional environments where anoxic bottom water prevails, i.e. where S represents a large fraction of the sediment redox capacity (Canfield, 1998; Raven et al., 2018). Yet other electrochemical alternatives have tended to focus on soil and surface environments (Kappler et al., 2004), but those approach are not well suited for sediment and rock samples. Those approaches therefore lack the degree of generality that we envision here.

Our goal is to develop an experimental solution that would allow to address a range of surface and lithospheric redox questions quantitatively and self-consistently. Specifically, we develop a reproducible and accurate protocol to determine the ΔO_2 of rocks and sediments characterized by a wide range of chemical compositions, under a specific set of experimental conditions. One particular technical issue we managed to overcome was to ensure that sulfur, a ubiquitous and multi-valence-state element, is oxidized to its terminal (S^{6+}) oxidation state and then trapped in solid form, ensuring the absolute nature of the measurement for this element in particular. We first provide an experimental definition for the redox capacity, and then describe an experimental protocol involving a high-temperature redox titration to determine the absolute, and mass specific, redox capacity of rocks and sediments. Finally, we assess the reliability (accuracy and reproducibility) of our method to quantify the ΔO_2 value of a range of reference materials, and of a suite of natural samples representative of both surface and deep Earth

environments.

2. Experimental design

We define the absolute redox capacity (ΔO_2) of a system as the amount of O_2 required to oxidize its redox-active elements to their highest attainable valence state under some reference condition. The reference condition adopted here is 850 °C under initial vacuum. The reference oxidized valence state is of course element specific, and it is C^{4+} , S^{6+} and Fe^{3+} for carbon, sulfur and iron, respectively. The method to measure the redox capacity (absolute and mass specific) relies on exchanging a measurable amount of pure O_2 at high temperature between an electron acceptor (oxygen source) and the sample (electron donor) under rigorously controlled experimental conditions. The high-temperature redox titration (HT-RT) process is applied to samples containing elements such as C, S, and Fe in any of their low-valence states.

The experimental design includes a quartz reaction tube containing two smaller quartz inserts (Fig. 1). All the parts are annealed at 900 °C overnight to remove potential contaminants such as organic compounds. One of those inserts (placed at the bottom of the reaction tube) contains the oxygen donor in the form of 0.5 mm CuO wires (product B1122 from Elemental Microanalysis, typically 60 mg). The other insert contains the powdered sample, typically 500 μg to 3 mg material, covered with a layer of powdered MgO (product 342793 from Sigma Aldrich). About $\sim 200 \mu g$ of quartz wool is inserted on top of the upper insert containing the sample/MgO (Fig. 1, Fig. 2A).

Despite the low melting point of Cu (1080 °C), which limits application of the method to below ~ 1000 °C, solid CuO was selected as an oxygen carrier because (1) it can maintain high partial pressure of O_2 gas at elevated temperature (Saha and Bhattacharya, 2011), (2) it is unreactive with the quartz insert, and, (3) it can be weighed precisely using a microbalance (MX 5 instrument by Mettler Toledo) before and after reaction. To prevent contamination from other unaccounted O_2 sources (e.g. air), the quartz tube is flame sealed under a vacuum of ca. 5 μbar (Fig. 1A). Another reason for conducting the measurement by redox titration using an oxygen carrier under vacuum (as opposed to a direct oxidation of the sample in air), is that the variation in mass of the sample will generally not be due to gain of O_2 only, but also to a range of devolatilization reactions. This is most evident for materials such as elemental C and S (see Table 2).

The assembly is then placed in an oven, heated to 850 °C, and maintained at peak temperature for a minimum of 7 h to allow for complete oxidation of the sample. At elevated T , the oxygen carrier disproportionates to form solid Cu_2O , Cu and O_2 according to:



and



A larger amount of CuO provides faster oxidation rate (higher partial pressure of O_2 in the reactor), especially for samples containing refractory C forms, such as graphitic materials. The oven is then left to cool down slowly (about 7 hours) to let Cu and Cu_2O recombine with the excess O_2 .

Under those conditions, the key for accurate weight loss measurement is that (i) the mass loss in the oxygen carrier container is due to loss of gaseous O_2 only, and that (ii) the excess O_2 is quantitatively recovered during the cooling stage.

The tube is then cracked open cleanly to avoid contamination of the inserts with broken shards of quartz. Test runs using $Al(OH)_3$ showed that H_2O lost by particularly hydrous samples during combustion may condense in the CuO insert upon cooling, preventing accurate weight loss determination. Therefore, all reactants are stored under moisture free conditions (MgO, CuO), and the inner CuO insert needs to be dried

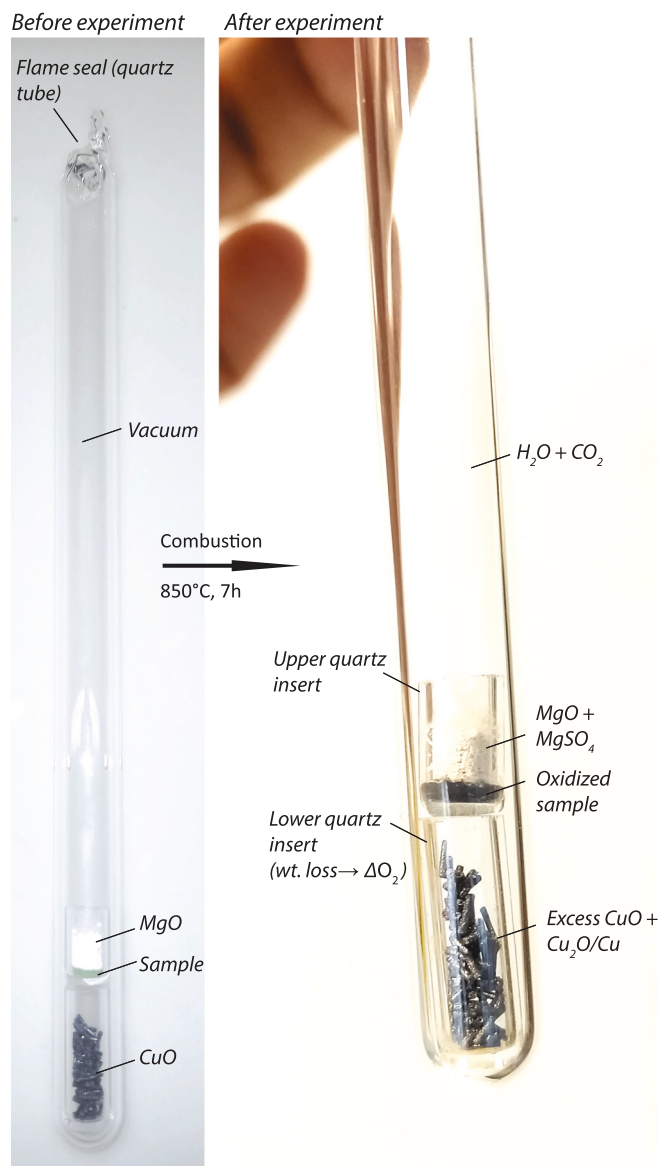


Fig. 1. Design of experimental assembly

gently after reaction, when hydrous samples are analyzed, until the mass has reached a constant value.

In practice, we determine the absolute redox capacity (ΔO_2) by weight loss of the insert containing the oxygen carrier:

$$\Delta O_2 = \frac{(w_i - w_o)}{M} \quad (3)$$

where w_i is the mass of the CuO container before experiment (Tables 2 and 3), w_o is the mass of the same container (containing various proportions of Cu, Cu₂O and excess CuO) after completion of the experiment, and $M = 32$ g/mol is the molar mass of O₂.

The mass specific redox capacity, dO_2 , is the amount of oxygen needed to oxidize one gram of sample to its reference state, and $dO_2 = \frac{\Delta O_2}{w_s}$, where w_s is the mass of the sample (in gram). Since C, S and Fe are the three dominant redox-sensitive elements in the crust and sediments, we applied the method to elemental C (disordered graphite powder, product 40798 from Alpha Aesar), pure Fe²⁺ compounds (natural siderite, ETH collection), synthetic magnetite (~Fe₃O₄), and native sulfur (product 213292 from Sigma-Aldrich) to test the reproducibility

and accuracy of our experimental procedure. For native sulfur, two configurations were tested, one with, and one without MgO powder, which serves as a S getter according to the reaction:



Hence, MgO protects CuO and Cu from interfering reactions with gaseous SO₂ or SO₃ susceptible to alter the weight loss measurement. In addition, the formation of MgSO₄ minerals ensures that S is oxidized its highest oxidation state, S⁶⁺. The requirement to synthesize MgSO₄ over the course of the reaction sets a temperature limit to the process to within 850–1000 °C. Here we have set our reference condition to 850 °C. This temperature ensures a good compromise between fast reaction kinetics, efficient trapping of S, and integrity of the CuO/Cu₂O/Cu solids inside the oxygen carrier insert.

Rock samples (Table 1) were selected to be representative of the various environments of the upper mantle, lower-, middle- and upper crust, as well as the Earth's surface.

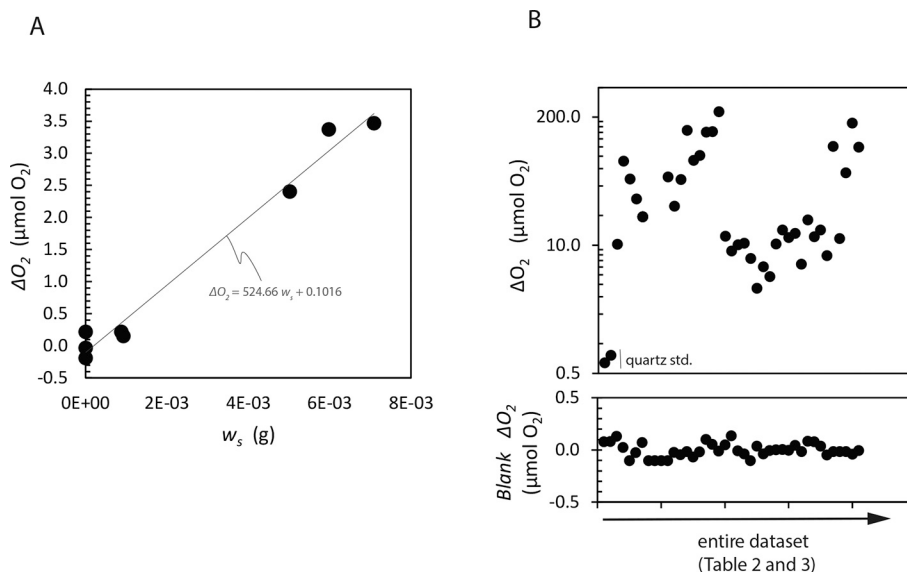


Fig. 2. A. Test of the protocol with CuO and quartz wool to derive the experimental blank, linking wool mass (w) and its associated absolute redox capacity (ΔO_2^{wool}). B. Upper panel shows the entire range of redox capacity values obtained for the data set. Lower panel shows the correction applied for each sample (ie. wool), highlighting the excellent blank for this protocol.

Table 1

List of samples analyzed in this study and some characteristics.

Sample ID	Rock class	Rock type	Provenance
KO0783	Ultramafic	Dunite	Kohistan (Pakistan)
KO0750	Lower crust plutonic	Garnet amphibolite	Kohistan (Pakistan)
KO0722	Lower crust plutonic	Garnet amphibolite	Kohistan (Pakistan)
KO07109	Middle crust plutonic	Gabbro-norite	Kohistan (Pakistan)
KO07121	Upper crust plutonic	Diorite	Kohistan (Pakistan)
s119	Metamorphic sediment	Calcareous schist	Nufenenpass, Swiss Alps
MSG9a	Unmetamorphosed sediment	Black shale	Monte San Giorgio, Swiss Alps
MLC	Unconsolidated lacustrine sediment	Sulfidic sediment	Lago Cadagno, Swiss Alps
KTB	Terrestrial sediment	Lignite	KTB borehole, Germany

3. Results

All results are reported in Table 2. The absolute blank obtained for an assembly containing only the inner oxygen carrier insert is excellent, usually below 500 nmol O_2 (Table 1 and Fig. 2). This ensures that the excess O_2 is fully recovered during the cooling stage. The procedural blank is estimated by measuring a pre-combusted powder of inclusion free Brazilian quartz (ie. non-oxidizable) for which we obtained $dO_2 < 40 \mu\text{mol/g}$ (Table 2, Fig 2B). This value may be ascribed to minor adsorption of residual O_2 in the fine powder or impurities. This means all values reported in Tables 2 and 3 may be slightly overestimated by ca. 50 $\mu\text{mol/g}$.

Runs using elemental C (Fig. 3) yielded $dO_2 = 85,830 \mu\text{mol O}_2/\text{g}$ (1SD = 1098 $\mu\text{mol O}_2/\text{g}$, $n = 6$) which lies within 5% of the theoretical value ($dO_2^* = 83,259 \mu\text{mol O}_2/\text{g}$). Small discrepancies may be related to impurities (e.g. reduced H radicals) and/or inherent analytical errors.

Replicate runs using natural siderite ($\text{Fe}^{2+}\text{CO}_3$), an ionic mineral, yielded $dO_2 = 2033 \mu\text{mol O}_2/\text{g}$ (1SD = 28 $\mu\text{mol O}_2/\text{g}$, $n = 3$) $\mu\text{mol O}_2/\text{g}$, which also shows good reproducibility and accuracy when compared to the theoretical value ($dO_2^* = 2156 \mu\text{mol O}_2/\text{g}$) (Fig. 4). This is also the

case for synthetic magnetite (Fig. 4), a mainly covalent bonded mineral, for which we obtained a value of 1096 $\mu\text{mol O}_2/\text{g}$, compared to a reference value measured at 1030 $\mu\text{mol O}_2/\text{g}$ (stoichiometric magnetite is at 1070 $\mu\text{mol O}_2/\text{g}$). This also demonstrates that the reliability of the method is independent of the mineralogical structure of the sample.

Measurements of sulfur-rich materials require special care. The values obtained for native sulfur were systematically offset compared to the target value $dO_2^* = 46,779 \mu\text{mol O}_2/\text{g}$ (Fig. 5). The interface between the CuO rods and the lower insert showed evidence of melting, probably resulting from the interaction between quartz, Cu and SO_2 produced during combustion. Adding a layer of MgO improved the outcome as the values ($dO_2 = 47,536$ (1SD = 1350) $\mu\text{mol O}_2/\text{g}$) compare well to the theoretical target. This result illustrates (i) that S is fully oxidized to its S^{6+} valence state, and (ii) that S is fully trapped within the MgO layer as Mg-sulfate. Interestingly, this strategy may allow isotopic characterization of the S provided it is locked quantitatively, i.e. as sulfate, but this development is beyond the scope of this study.

4. Discussion

4.1. Redox structure of the lithosphere

Preliminary applications of the method to samples selected to represent different surface or deep Earth environments highlight an interesting feature of the lithospheric redox structure.

Rocks with relatively low dO_2 , typically lower than 500 $\mu\text{mol O}_2/\text{g}$ tend to predominate in the crystalline crust and upper mantle (Fig. 6), while rocks characterized by elevated dO_2 , typically sedimentary rocks with dO_2 exceeding 30,000 $\mu\text{mol O}_2/\text{g}$, are pervasive in the surface environment. This feature hinges, in part, on the ability of C (e.g. elemental C, CH_4) and S (e.g. elemental S, H_2S) to donate up to 8 electrons (as opposed to 1 electron for Fe), to reach their reference (oxidized) valence state, and to the low atomic mass of these volatiles. Nevertheless, this redox structure does seem to contrast with the notion that the μO_2 in the upper mantle is low, and therefore highly reducing compared to the surface environment (Frost and McCammon, 2008; McCammon, 2005). Yet, this paradox is only apparent since the thermodynamic activity of O_2 in a system is in general unrelated to the absolute abundance of redox elements, but rather to the nature of the phase assemblage and to the local environmental conditions, chiefly P

Table 2

Experimental results obtained in the development stage of the method, including blank assessment, test with elemental carbon, elemental sulfur and siderite.

#run	Nature of sample	Initial OC cap wt. (w_i , mg)	Initial spl. wt. (w_s , mg)	Weight MgO (mg)	Final OC cap wt. (w_o , mg)	Δw (μg)	ΔO_2 ($\mu\text{mol O}_2$)	dO_2 ($\mu\text{mol O}_2/\text{g}$)
18	CuO + wool	548.679	5.022	0.000	548.602	77	2.4	479
19	CuO + wool	463.028	5.977	0.000	462.920	108	3.4	565
20	CuO	530.642	0.000	0.000	530.648	-6	-0.2	-
21	CuO	547.758	0.000	0.000	547.751	7	0.2	-
120	CuO	796.665	0.000	0.000	796.666	-1	0.0	-
22	CuO + wool	725.897	0.929	0.000	725.892	5	0.2	168
23	CuO + wool	482.595	0.875	0.000	482.588	7	0.2	250
24	CuO + wool	480.854	7.091	0.000	480.743	111	3.5	489
126	Quartz	766.226	19.884	0.000	766.203	23	0.7	36
138	Quartz	808.798	21.715	0.000	808.771	27	0.8	39
27	Elemental C	573.621	0.121	0.000	573.290	331	10.3	85,486
28	Elemental C	562.482	0.829	0.000	560.196	2286	71.4	86,173
78	Elemental C	738.833	0.555	0.000	737.333	1500	46.9	84,459
89	Elemental C	658.276	0.348	0.000	657.331	945	29.5	84,860
91	Elemental C	855.011	0.221	0.000	854.387	624	19.5	88,235
59	Native S	731.084	3.252	0.000	732.940	-1856	-58.0	-17,835
60	Native S	544.684	0.963	0.000	545.207	-523	-16.3	-16,972
67	Native S	759.171	2.507	0.000	760.300	-1129	-35.3	-14,073
61	Native S	645.617	1.047	-	644.041	1576	49.3	47,039
62	Native S	652.161	0.506	6.009	651.363	798	24.9	49,284
73	Native S	770.942	0.971	5.881	769.458	1484	46.4	47,760
74	Native S	872.949	2.953	8.991	868.237	4712	147.2	49,865
80	Native S	753.265	1.446	10.527	750.942	2323	72.6	50,203
114	Native S	880.420	1.762	3.098	877.803	2617	81.8	46,414
115	Native S	900.949	3.112	4.320	896.449	4500	140.6	45,188
159	Native S	887.464	2.954	11.725	882.904	4560	142.5	48,240
160	Native S	888.737	4.816	9.823	881.448	7289	227.8	47,297
161	Synthetic magnetite	831.431	11.008	0.000	831.035	396	12.4	1124
162	Synthetic magnetite	813.885	8.142	3.468	813.601	284	8.9	1090
88	Siderite	598.729	5.035	0.000	598.406	323	10.1	2005
90	Siderite	778.760	5.038	0.000	778.426	334	10.4	2072
92	Siderite	838.926	3.568	0.000	838.695	231	7.219	2023
Δw (μg)	$\Delta w = (w_o - w_i) \times 10^3$, when w_o and w_i are expressed in milligrams.							
ΔO_2 ($\mu\text{mol O}_2$)	Absolute redox capacity, $\Delta O_2 = \Delta w / M$, with M the molar mass of O_2 , and Δw is in micrograms.							
dO_2 ($\mu\text{mol O}_2/\text{g}$)	Mass specific redox capacity, $dO_2 = \Delta O_2 / w_s$							

Table 3

Experimental results obtained for selected natural materials.

#run	Nature of sample	Rock type	Initial OC cap wt. (w_i , mg)	Initial spl. wt. (w_s , mg)	weight MgO (mg)	Final OC cap wt. (w_o , mg)	Δw (μg)	ΔO_2 ($\mu\text{mol O}_2$)	dO_2 ($\mu\text{mol O}_2/\text{g}$)
33	KO0783	UM	529.690	21.038	0.000	529.572	118	3.7	175
57	KO0783	UM	555.712	29.171	0.000	555.520	192	6.0	206
58	KO0783	UM	506.304	21.138	0.000	506.150	154	4.8	228
31	KO0750 (1)	LC	520.076	24.045	0.000	519.747	329	10.3	428
47	KO0750 (2)	LC	207.013	25.687	0.000	206.556	457	14.3	556
48	KO0750 (3)	LC	493.314	30.051	0.000	492.931	383	12.0	398
77	KO0750 (4)	LC	820.912	37.273	7.680	820.489	423	13.2	355
32	KO0722	LC	539.599	35.465	0.000	539.394	205	6.4	181
37	KO07109	MC	527.891	64.700	0.000	527.309	582	18.2	281
35	KO07121	UC	653.185	26.726	0.000	652.791	394	12.3	461
53	s119 (1)	sed	493.939	17.876	0.000	493.481	458	14.3	801
54	s119 (2)	sed	498.503	9.528	0.000	498.254	249	7.8	817
87	MSG9a	sed	774.476	2.642	3.087	771.252	3224	100.7	38,134
83	MLC	sed	756.141	0.615	5.426	755.767	374	11.7	19,004
55	KTB (1)	sed	524.033	1.048	0.000	522.292	1741	54.4	51,914
56	KTB (2)	sed	583.474	3.408	0.000	577.900	5574	174.2	51,111
64	KTB (3)	sed	826.336	1.841	9.185	823.171	3165	98.9	53,724
Δw (μg)	$\Delta w = (w_o - w_i) \times 10^3$, when w_o and w_i are expressed in milligrams.								
ΔO_2 ($\mu\text{mol O}_2$)	Absolute redox capacity, $\Delta O_2 = \Delta w / M$, with M the molar mass of O_2 , and Δw is in micrograms.								
dO_2 ($\mu\text{mol O}_2/\text{g}$)	Mass specific redox capacity, $dO_2 = \Delta O_2 / w_s$								

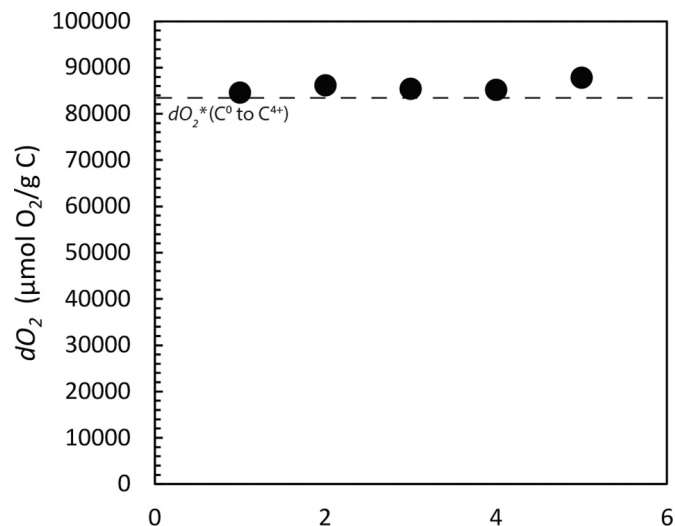


Fig. 3. Mass specific redox capacity, dO_2 , obtained for elemental carbon, compared to the theoretical value (dO_2^*).

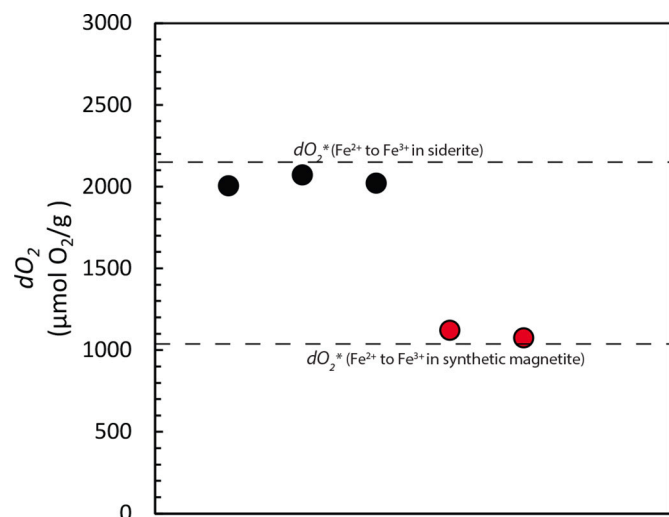


Fig. 4. Mass specific redox capacity, dO_2 , obtained for siderite ($FeCO_3$), and synthetic magnetite, compared to their theoretical values (dO_2^*).

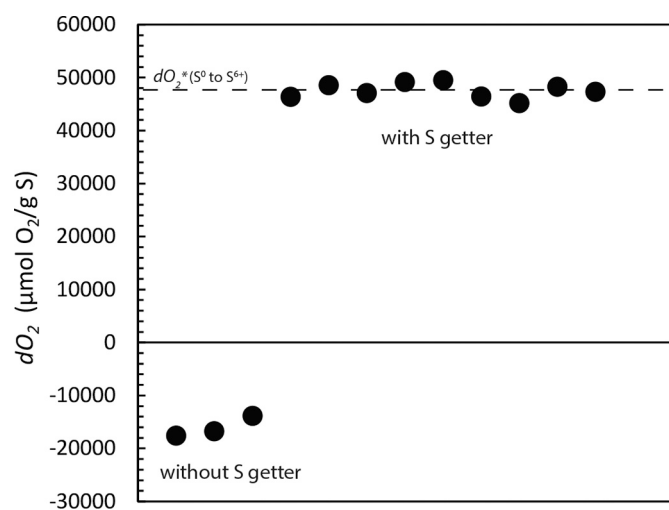


Fig. 5. Mass specific redox capacity, dO_2 , obtained for elemental sulfur, with and without MgO serving a S getter, compared to the theoretical value (dO_2^*).

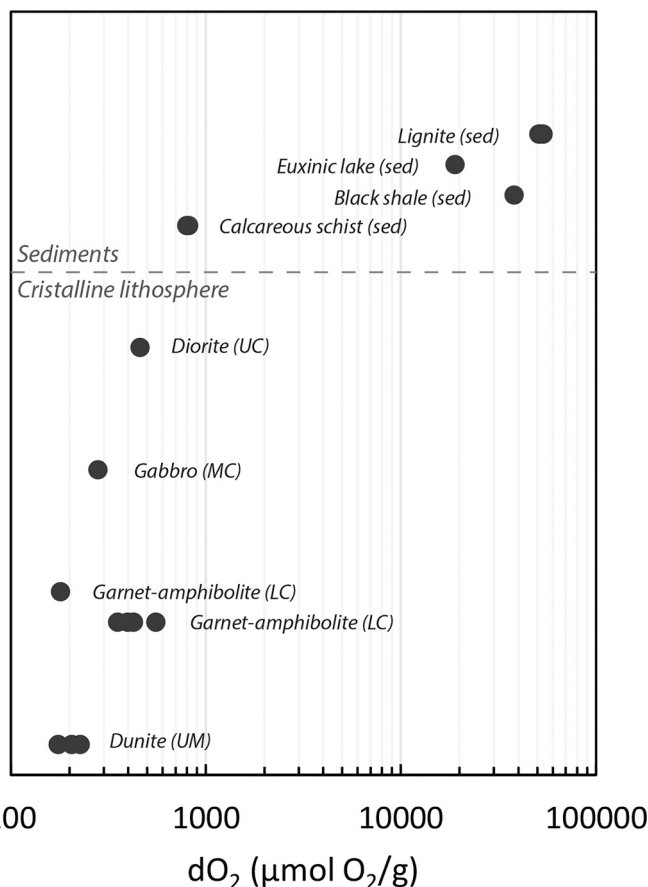


Fig. 6. Values of mass specific redox capacity obtained for representative rock types from the upper mantle to surface environment (cf. Table 1 and 3).

and T (Wood et al., 1990). Instead, the ability of biological processes to decouple reductants (e.g. S, C) from oxidants (e.g. O_2) in the surface environment (Falkowski and Godfrey, 2008), together with the efficiency of sedimentary processes to prevent their immediate recombination (Galvez, 2020), may play the key role in shaping this peculiar redox structure. Clearly, more work is needed to investigate the distribution of reductants in various surface environments and deep lithospheric settings, and assess whether this distribution has changed through time.

4.2. Geological applications

We envisage a range of potential applications for this type of measurement. First, estimates of paleoenvironmental redox conditions (Falkowski et al., 2008; Moore et al., 2017) have relied on changes in the immobilization of redox-sensitive elements (e.g. C, N, S, Fe, Zn, Mo, ...) in sediments (Tribovillard et al., 2006), and/or on the differential preservation of organic biomarkers (Anderson et al., 2019). However, these approaches are sensitive to distinct oxygenation thresholds, and usually clustered towards the reducing end of the spectrum. As such, they do not allow reconstructing past changes along the entire range of redox conditions observed at the Earth's surface. In this context, the ΔO_2 metric may offer a larger spectrum of investigation, as well as a more nuanced and self-consistent approach to address the issue. For example, it may help assessing how changes in subsurface ocean oxygenation relate to changes in respiratory carbon storage during Plio-Pleistocene glacial-interglacial cycles (Jaccard and Galbraith, 2012; Jaccard et al., 2016; Jacobel et al., 2019).

Second, the method may help quantify various processes of redox

partitioning associated with the sedimentary and plate-tectonic cycles. For example, while the sequestration of photosynthesized organic C (C^0) in marine sediments is widely recognized as the dominant O_2 source on geological timescales (Galvez, 2020; Berner, 1982; Hayes and Waldbauer, 2006), the burial of reduced S plays the same qualitative role but it has proved more tricky to quantify. This is because S occurs in multiple oxidation states in various phases: pyrite (FeS_2), pyrrhotite ($Fe_xS_{(1-x)}$), organic S, elemental S etc. As a result, various indirect and often semi-quantitative approaches have been taken to tie S burial to C burial (Berner, 1982) or, alternatively, to the abundance of reactive Fe in the rock (Canfield, 2004). Solving this question would bring us one step closer to determining whether hydrothermal weathering of the oceanic lithosphere (a net sink of O_2 on geological timescale, Hayes and Waldbauer 2006, Evans, 2012, Galvez, 2020) is offset by the burial and subduction of reduced C and S in deep-sea sediments (a net source of O_2) and, therefore, determine whether subduction zones are, or not, redox neutral (Evans, 2012, Galvez, 2020).

4.3. Accuracy of the method and future development

In contrast to other approaches requiring complex analytical infrastructure and a combination of distinct measurements, our method is cost- and relatively time effective, and applicable to a wide range of materials. Its main advantage is its self-consistency, providing a measure of a system's redox (electron-donor) capacity via a standard protocol, with experimentally defined reference conditions, and with a single approach regardless of the redox element considered.

However, the method may be improved in the future. For example, while we have shown that the disproportionation of CuO promotes oxidation of FeO, C and S to their highest oxidation state under the experimental conditions, this may not be the case for an important redox/sensitive oxide such as MnO (data not shown), an element relevant for recent or ancient marine environments (Johnson et al., 2013; Schissel and Aro, 1992; Tumiati et al., 2015). Therefore, a systematic study of a suite of minor or trace metal oxides that are also redox-sensitive in a range of surface end deep Earth environments (e.g. MnO, NiO, CoO, CrO) is indicated.

Moreover, in its current standard design, the method does not allow isolating the fractional contribution of each redox-sensitive element to the total redox capacity of the sample. This aspect may be explored in the future.

5. Conclusion

We have designed a self-consistent analytical procedure that allows measuring the redox capacity of rocks and sediments. It relies on a novel high-temperature redox titration protocol involving a solid-state oxygen donor (CuO). We have demonstrated the accuracy and reproducibility of this method for Fe, S and C, by far the more important redox active elements in sedimentary and crystalline rocks.

Preliminary applications of the method to a suite of rock materials showed orders of magnitude differences in redox capacity between typical upper mantle rocks and carbonaceous sediments. Kinetic and thermodynamic processes are jointly responsible for this complex redox structure.

Declaration of Competing Interest

The authors declare that they have no known competing financial interests or personal relationships that could have appeared to influence the work reported in this paper.

Acknowledgments

This project was supported through a Branco Weiss/Society in Science fellowship, ETH Zurich (M.E.G.).

M.E.G. and S.L.J. conceived the project. M.E.G. developed the experimental protocol, performed the experiments, analyzed the data, and wrote the paper with writing and editing contribution from S.L.J. M. E.G acknowledges partial funding from an installation fund to Olivier Bachmann, and S.L.J acknowledges funding from the Swiss National Science Foundation (grant PP00P2_172915). M.E.G. is indebted to J. Connolly and P. Ulmer at the IGP (ETH Zurich) for inspiring discussions and to Craig Manning and Bob Newton for introducing him to the beauty and potential of precision weight loss measurements. We thank P. Ulmer for providing the synthetic magnetite standard, O. Muntener for providing access to his collection of crustal material from Kohistan (Pakistan), T. Eglinton for access to his vacuum line, as well as Daniel Montluçon, Negar Haghypour, John Viaud-Murat and Nathan Karlewski for laboratory assistance. The thorough reviews by Bruno Scaillet and an anonymous reviewer improved the presentation of this work.

References

- Alt, J.C., et al., 2007. Hydrothermal alteration and microbial sulfate reduction in peridotite and gabbro exposed by detachment faulting at the Mid-Atlantic Ridge, 15° 20' N (ODP Leg 209): a sulfur and oxygen isotope study. *Geochem. Geophys. Geosyst.* 8 (8).
- Anderson, R.F., et al., 2019. Deep-sea oxygen depletion and ocean carbon sequestration during the last ice age. *Glob. Biogeochem. Cycles* 33 (3), 301–317.
- Arculus, R.J., 1985. Oxidation status of the mantle: past and present. *Annu. Rev. Earth Planet. Sci.* 13 (1), 75–95.
- Berner, R.A., 1982. Burial of organic carbon and pyrite sulfur in the modern ocean: its geochemical and environmental significance. *Am. J. Sci.* 282.
- Berry, A.J., Stewart, G.A., O'Neill, H.S.C., Mallmann, G., Mosselmans, J.F.W., 2018. A re-assessment of the oxidation state of iron in MORB glasses. *Earth Planet. Sci. Lett.* 483, 114–123.
- Bézos, A., Humler, E., 2005. The $Fe^{3+}/\Sigma Fe$ ratios of MORB glasses and their implications for mantle melting. *Geochim. Cosmochim. Acta* 69 (3), 711–725.
- Borch, T., Kretzschmar, R., Kappler, A., Cappellen, P.V., Ginder-Vogel, M., Voegelin, A., Campbell, K., 2010. Biogeochemical Redox Processes and their Impact on Contaminant Dynamics. *Environ. Sci. Technol.* 44, 15–23.
- Brounce, M., Cottrell, E., Kelley, K.A., 2019. The redox budget of the Mariana subduction zone. *Earth Planet. Sci. Lett.* 528, 115859.
- Canfield, D.E., 1998. A new model for Proterozoic ocean chemistry. *Nature* 396 (6710), 450–453.
- Canfield, D.E., 2004. The evolution of the Earth surface sulfur reservoir. *Am. J. Sci.* 304 (10), 839–861.
- Canfield, D.E., Raiswell, R., Westrich, J.T., Reaves, C.M., Berner, R.A., 1986. The use of chromium reduction in the analysis of reduced inorganic sulfur in sediments and shales. *Chem. Geol.* 54 (1), 149–155.
- Catling, D., 2014. The Great Oxidation Event Transition.
- Connolly, J., 1995. Phase diagram methods for graphitic rocks and application to the system C–O–H–FeO–TiO₂–SiO₂. *Contrib. Mineral. Petrol.* 119 (1), 94–116.
- Debret, B., et al., 2017. Assessing sulfur redox state and distribution in abyssal serpentinites using XANES spectroscopy. *Earth Planet. Sci. Lett.* 466, 1–11.
- Evans, B.W., Dyar, M.D., Kuehner, S.M., 2012. Implications of ferrous and ferric iron in antigorite. *Am. Mineral.* 97 (1), 184–196.
- Evans, K.A., 2006. Redox decoupling and redox budgets: conceptual tools for the study of earth systems. *Geology* 34 (6), 489–492.
- Evans, K.A., 2012. The redox budget of subduction zones. *Earth Sci. Rev.* 113 (1–2), 11–32.
- Falkowski, P.G., Godfrey, L.V., 2008. Electrons, life and the evolution of Earth's oxygen cycle. *Philos. Trans. R. Soc. B Biol. Sci.* 363 (1504), 2705–2716.
- Falkowski, P.G., Fenchel, T., Delong, E.F., 2008. The microbial engines that drive earth's biogeochemical cycles. *Science* 320 (5879), 1034–1039.
- Frost, D.J., McCammon, C.A., 2008. The Redox state of earth's mantle. *Annu. Rev. Earth Planet. Sci.* 36 (1), 389–420.
- Galvez, Matthieu E., 2020. Redox constraints on a Cenozoic imbalance in the organic carbon cycle. *Am. J. Sci.* 320 (8), 730–751 arXiv: 2005.02806.
- Galvez, M.E., Fischer, W.W., Jaccard, S.L., et al., 2020. Materials and pathways of the organic carbon cycle through time. *Nat. Geosci.* 13, 535–546.
- Hayes, J.M., Waldbauer, J.R., 2006. The carbon cycle and associated redox processes through time. *Philos. Trans. R. Soc. Lond. Ser. B Biol. Sci.* 361 (1470), 931–950.
- Holland, H.D., 2002. Volcanic gases, black smokers, and the Great Oxidation Event. *Geochim. Cosmochim. Acta* 66 (21), 3811–3826.
- Jaccard, S.L., Galbraith, E.D., 2012. Large climate-driven changes of oceanic oxygen concentrations during the last deglaciation. *Nat. Geosci.* 5 (2), 151–156.
- Jaccard, S.L., Galbraith, E.D., Martínez-García, A., Anderson, R.F., 2016. Covariation of deep Southern Ocean oxygenation and atmospheric CO₂ through the last ice age. *Nature* 530 (7589), 207.
- Jacobel, A., et al., 2019. Deep Pacific storage of respired carbon during the last ice age: perspectives from bottom water oxygen reconstructions. *Quat. Sci. Rev.* 106065.
- Johnson, J.E., et al., 2013. Manganese-oxidizing photosynthesis before the rise of cyanobacteria. *Proc. Natl. Acad. Sci.* 110 (28), 11238–11243.

- Jugo, P.J., Wilke, M., Botcharnikov, R.E., 2010. Sulfur K-edge XANES analysis of natural and synthetic basaltic glasses: Implications for S speciation and S content as function of oxygen fugacity. *Geochim. Cosmochim. Acta* 74 (20), 5926–5938.
- Kappler, A., Benz, M., Schink, B., Brune, A., 2004. Electron shuttling via humic acids in microbial iron(III) reduction in a freshwater sediment. *FEMS Microbiol. Ecol.* 47, 85–92.
- Kleidon, A., 2010. Non-equilibrium thermodynamics, maximum entropy production and Earth-system evolution. *Philos. Trans. R. Soc. A Math. Phys. Eng. Sci.* 368 (1910), 181–196.
- McCammon, C., 2005. The Paradox of Mantle Redox. *Science* 308 (5723), 807–808.
- Moore, E.K., Jelen, B.I., Giovannelli, D., Raanan, H., Falkowski, P.G., 2017. Metal availability and the expanding network of microbial metabolisms in the Archaean eon. *Nat. Geosci.* 10 (9), 629–636.
- Morse, J.W., Cornwell, J.C., 1987. Analysis and distribution of iron sulfide minerals in recent anoxic marine sediments. *Mar. Chem.* 22 (1), 55–69.
- O'Neill, H.S.C., Berry, A.J., Mallmann, G., 2018. The oxidation state of iron in Mid-Ocean Ridge Basaltic (MORB) glasses: Implications for their petrogenesis and oxygen fugacities. *Earth Planet. Sci. Lett.* 504, 152–162.
- Perks, Helen M., Keeling, Ralph F., 1998. A 400 kyr record of combustion oxygen demand in the western equatorial Pacific: Evidence for a precessionally forced climate response. *Paleoceanography* 13 (1), 63–69.
- Perks, Helen M., Charles, Christopher D., Keeling, Ralph F., 2002. Precessionally forced productivity variations across the equatorial Pacific. *Paleoceanography* 17 (3), 9–10.
- Raven, M.R., et al., 2018. Organic carbon burial during OAE2 driven by changes in the locus of organic matter sulfurization. *Nat. Commun.* 9 (1), 3409.
- Rimmer, D.L., 2006. Free radicals, antioxidants, and soil organic matter recalcitrance. *Eur. J. Soil Sci.* 57, 91–94.
- Saha, C., Bhattacharya, S., 2011. Comparison of CuO and NiO as oxygen carrier in chemical looping combustion of a Victorian brown coal. *Int. J. Hydrog. Energy* 36 (18), 12048–12057.
- Schissel, D., Aro, P., 1992. The major early Proterozoic sedimentary iron and manganese deposits and their tectonic setting. *Econ. Geol.* 87 (5), 1367–1374.
- Tribouillard, N., Algeo, T.J., Lyons, T., Riboulleau, A., 2006. Trace metals as paleoredox and paleoproductivity proxies: an update. *Chem. Geol.* 232 (1–2), 12–32.
- Tumiati, S., Godard, G., Martin, S., Malaspina, N., Poli, S., 2015. Ultra-oxidized rocks in subduction mélanges? Decoupling between oxygen fugacity and oxygen availability in a Mn-rich metasomatic environment. *Lithos* 226, 116–130.
- Waldo, G.S., Carlson, R.M., Moldowan, J.M., Peters, K.E., Penner-Hahn, J.E., 1991. Sulfur speciation in heavy petroleum: information from X-ray absorption near-edge structure. *Geochim. Cosmochim. Acta* 55 (3), 801–814.
- Waychunas, G.A., Apte, M.J., Brown, G.E., 1983. X-ray K-edge absorption spectra of Fe minerals and model compounds: near-edge structure. *Phys. Chem. Miner.* 10 (1), 1–9.
- Wilke, M., Farges, F., Petit, P.-E., Brown Jr., G.E., Martin, F., 2001. Oxidation state and coordination of Fe in minerals: an Fe K-XANES spectroscopic study. *Am. Mineral.* 86 (5–6), 714–730.
- Wood, B.J., Bryndzia, L.T., Johnson, K.E., 1990. Mantle oxidation state and its relationship to tectonic environment and fluid speciation. *Science* 248 (4953), 337–345.